CHEMISTRY OF MATERIALS
Article

Chem. Mater. **2010,** *22,* 3599–3609 3599
DOI:10.1021/cm1009042

Eu^{3+}-Assisted Short-Range Ordering of Photoluminescent Bridged Silsesquioxanes

Sónia S. Nobre,[†,‡] Xavier Cattoën,[‡] Rute A. S. Ferreira,[†] Carole Carcel,[‡] Verónica de Zea Bermudez,*[,§] Michel Wong Chi Man,*[,‡] and Luis D. Carlos*[,†]

[†]*Department of Physics, CICECO, University of Aveiro, 3810-193 Aveiro, Portugal,* [‡]*Institut Charles Gerhardt Montpellier, UMR 5253 CNRS-UM2-ENSCM-UM1, Ecole Nationale Supérieure de Chimie de Montpellier, 8 rue de l'école normale, 34296 Montpellier Cedex 5, France, and* [§]*Department of Chemistry, CQ-VR, University of Trás-os-Montes e Alto Douro, 5001-801 Vila Real, Portugal*

Received March 30, 2010. Revised Manuscript Received May 12, 2010

The bridged silsesquioxane precursor $(EtO)_3Si(CH_2)_3NH(C{=}O)NH\text{-}(CH_2)_{12}\text{-}NH(C{=}O)NH\text{-}(CH_2)_3\ Si(OEt)_3$, combining polymerizable silylated groups, urea functionalities, and alkyl chains, undergoes fluoride (F^-)-catalyzed sol−gel reactions in the presence or absence of $EuCl_3 \cdot 6H_2O$. Supramolecular self-assembly of the growing structure relies primarily on the establishment of strong and ordered hydrogen bonding interactions. In the case of the Eu^{3+}-containing hybrids the lanthanide ions play a totally unparallel dual-role acting simultaneously as structure directing agents and structural probes to sense locally morphological alterations. In the early stages of the synthesis, while a fraction of the Eu^{3+} ions promotes the formation of a unidirectional urea−urea hydrogen-bonded array, the remaining ions coordinate to silanol (Si−OH) groups inhibiting the growth of the siloxane network and yielding small anisotropic flakes (∼200 nm long). These are subsequently assembled on the micrometer scale in a brick-like tile-to-tile arrangement that ends up with the formation of fibers or twisted bundles (3.0−4.0 μm long and 0.5−1.0 μm wide). At higher Eu^{3+} concentrations, Eu^{3+}-based ionic interfiber cross-links hinder the solvent flow and force adjacent fibers to adopt a bow-tie form (3.0−4.0 μm long and 3.0 μm wide at the tips). The hybrids are room temperature multiwavelength emitters because of the convolution of the hybrids' intrinsic emission and the Eu^{3+} intra-$4f^6$ transitions. The photoluminescence features ($^5D_0 \rightarrow {}^7F_0$ energy, $^5D_0$ quantum efficiency, number of coordinated water molecules, and experimental intensity parameters) as a function of the Eu^{3+} content and acidic- and F^--catalyzed conditions used in the synthesis are compared to address the effect of the morphology in the photoluminescence features of the hybrid materials.

Introduction

Functional organic−inorganic hybrid materials with improved or unusual features have received considerable attention in the past few years. Their rational design through bottom-up approaches, especially soft inorganic chemistry routes such as the sol−gel method,[1−3] relying on the appropriate choice of hybrid nano-objects (nanobuilding blocks, NBBs), permits to tailor the properties over broad length scales (from the atomic to the mesoscopic and macroscopic levels) with the consequent impact in diverse fields (e.g., photonics, microelectronics and micro-optics, catalysis, smart coatings, cosmetics, energy, and biomedicine).[4−7] In particular, the interest in lanthanide (Ln^{3+})-containing organic−inorganic hybrids has grown considerably during the past decade because of their potential applications as optically active components in photonic and biophotonic devices; for recent reviews see references 8−11.

In the past few years the combination of sol−gel reactions with self-assembly strategies[12−16] or molecular

*To whom correspondence should be addressed. E-mail: lcarlos@ua.pt (L.D.C.), michel.wong-chi-man@enscm.fr (M.W.C.M.), vbermude@utad.pt (V.d.Z.B). Fax: +351 234 378197 (L.D.C.), +33 467144 353 (M.W.C.M.), +351 259 350480 (V.d.Z.B). Phone: +351 234 370946 (L.D.C.), +33 467 147 219 (M.W.C.M.), +351 259 350253 (V.d.Z.B).

(1) Hench, L. L.; West, J. K. *Chem. Rev.* **1990**, *90*, 33–72.
(2) Sanchez, C.; Ribot, F. *New. J. Chem.* **1994**, *18*, 1007–1047.
(3) Schmidt, H. *J. Sol-Gel Sci. Technol.* **2006**, *40*, 115–130.
(4) Schottner, G. *Chem. Mater.* **2001**, *13*, 3422–3435.
(5) Sanchez, C.; Lebeau, B. *MRS Bull.* **2001**, *26*, 377–387.
(6) Sanchez, C.; Lebeau, B.; Chaput, F.; Boilot, J. P. *Adv. Mater.* **2003**, *15*, 1969–1994.
(7) Sanchez, C.; Julian, B.; Belleville, P.; Popall, M. *J. Mater. Chem.* **2005**, *15*, 3559–3592.
(8) Escribano, P.; Julián-López, B.; Planelles-Aragó, J.; Cordoncillo, E.; Viana, B.; Sanchez, C. *J. Mater. Chem.* **2008**, *18*, 23–40.
(9) Carlos, L. D.; Ferreira, R. A. S.; de Zea Bermudez, V.; Ribeiro, S. J. L. *Adv. Mater.* **2009**, *21*, 509–534.
(10) Comby, S.; Bünzli, J. C. G. In *Handbook on the Physics and Chemistry of Rare Earths*. Gschneider, K. A., Jr, Bünzli, J. C. G., Pecharsky, V. K., Eds.; Elsevier Science: New York, 2007; Vol. *37*, p 217.
(11) Binnemans, K. *Chem Rev* **2009**, *109*, 4283–4374.
(12) Moreau, J. J. E.; Vellutini, L.; Wong Chi Man, M.; Bied, C.; Bantignies, J. L.; Dieudonné, P.; Sauvajol, J. L. *J. Am. Chem. Soc.* **2001**, *123*, 7957–7958.
(13) Liu, N. G.; Yu, K.; Smarsly, B.; Dunphy, D. R.; Jiang, Y. B.; Brinker, C. J. *J. Am. Chem. Soc.* **2002**, *124*, 14540–14541.
(14) Yang, Y. G.; Nakazawa, M.; Suzuki, M.; Kimura, M.; Shirai, H.; Hanabusa, K. *Chem. Mater.* **2004**, *16*, 3791–3793.

© 2010 American Chemical Society
Published on Web 05/26/2010

Scheme 1. Synthesis of Amorphous (A12) and Lamellar (L12) Organic-Inorganic Hybrids

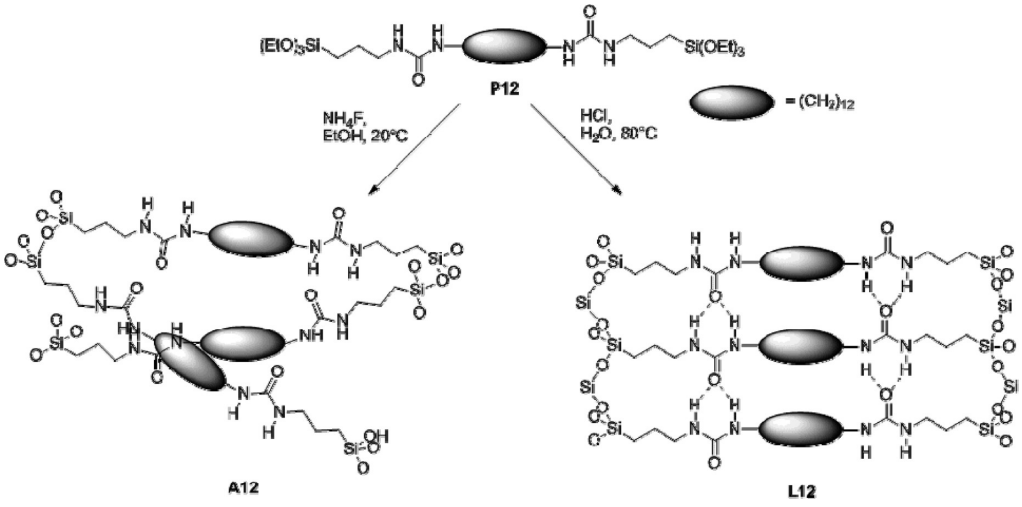

recognition principles[17] have been successfully explored to produce sophisticated and complex hierarchically structured organic−inorganic hybrid systems. Highly organized hybrids with well-defined morphologies on the macroscopic scale and controlled nanostructures were synthesized from diurea cross-linked silsesquioxanes[12,18−22] and monoamide cross-linked alkylsilanes.[23] The challenging underlying concept (called *self-directed assembly*) relies essentially on the establishment of weak hydrophobic interactions between the alkyl chains and on the ability of adjacent amide/urea groups to self-assemble through strong/very strong hydrogen bonding interactions. These interactions lead to the creation of a hydrogen-bonded array that plays itself the role of internal template directing the growth of the supramolecular architecture.

The organization of hybrid silicas depends critically on the synthetic procedure. In the case of the diurea cross-linked alkyl-based silsesquioxane precursor including a dodecyl chain (**P12**) the use of an acid catalyst (hydrochloric acid, HCl) and a large excess of water (R (mol mol^{-1}) = H_2O/Si = 300) induced the formation of a crystalline lamellar structure (**L12**).[12,19−21] In contrast, when ammonium fluoride (NH_4F) catalyst was used in ethanol (EtOH) medium with stoichiometric amounts of water ($R = 3$) an amorphous material (**A12**) was obtained (Scheme 1).[20]

The various examples reported in the literature of the organization and texturing of Ln^{3+}-doped organic−inorganic hybrids templated by structure-directing agents involved essentially mesostructured materials based on zeolites,[24] silicas (MCM-41, MCM-48 and SBA-15),[25−27] and functional organosilanes.[28−30] The only references to Eu^{3+}-doped self-directed assembled organic−inorganic materials regard lamellar diurea **Eu@L12** silsesquioxanes[31] and monoamidosils[32] obtained very recently.

In the present work we report the role played by the Eu^{3+} ions in the modulation of the morphology and size of the **Eu@A12** hybrids *via quasi*-inhibition (i.e., marked reduction) of the growth rate along preferential directions of the siloxane network formed through sol−gel reactions and urea-mediated supramolecular self-assembly. The Eu^{3+}-modified inorganic framework growth kinetics affects growth shape resulting in the formation of primary ∼200 nm-long plates which first pile up in a brick-like fashion that mimics the nacre structure,[33,34] and then

(15) Alauzun, J.; Mehdi, A.; Reyé, C.; Corriu, R. J. P. *J. Mater. Chem.* **2005**, *15*, 841–843.
(16) Shimojima, A.; Goto, R.; Atsumi, N.; Kuroda, K. *Chem. Eur. J.* **2008**, *14*, 8500–8506.
(17) Arrachart, G.; Creff, G.; Wadepohl, H.; Blanc, C.; Bonhomme, C.; Babonneau, F.; Alonso, B.; Bantignies, J. L.; Carcel, C.; Moreau, J. J. E.; Dieudonné, P.; Sauvajol, J. L.; Massiot, D.; Wong Chi Man, M. *Chem. Eur. J.* **2009**, *15*, 5002–5005.
(18) Moreau, J. J. E.; Pichon, B. P.; Wong Chi Man, M.; Bied, C.; Pritzkow, H.; Bantignies, J. L.; Dieudonné, P.; Sauvajol, J. L. *Angew. Chem., Int. Ed.* **2004**, *43*, 203–206.
(19) Moreau, J. J. E.; Vellutini, L.; Dieudonné, P.; Wong Chi Man, M.; Bantignies, J. L.; Sauvajol, J. L.; Bied, C. *J. Mater. Chem.* **2005**, *15*, 4943–4948.
(20) Moreau, J. J. E.; Vellutini, L.; Wong Chi Man, M.; Bied, C.; Dieudonné, P.; Bantignies, J. L.; Sauvajol, J. L. *Chem. Eur. J.* **2005**, *11*, 1527–1537.
(21) Bantignies, J. L.; Vellutini, L.; Maurin, D.; Hermet, P.; Dieudonné, P.; Wong Chi Man, M.; Bartlett, J. R.; Bied, C.; Sauvajol, J. L.; Moreau, J. J. E. *J. Phys. Chem. B* **2006**, *110*, 15797–15802.
(22) Dieudonné, P.; Wong Chi Man, M.; Pichon, B. P.; Vellutini, L.; Bantignies, J. L.; Blanc, C.; Creff, G.; Finet, S.; Sauvajol, J. L.; Bied, C.; Moreau, J. J. E. *Small* **2009**, *5*, 503–510.
(23) Carlos, L. D.; de Zea Bermudez, V.; Amaral, V. S.; Nunes, S. C.; Silva, N. J. O.; Ferreira, R. A. S.; Rocha, J.; Santilli, C. V.; Ostrovskii, D. *Adv. Mater.* **2007**, *19*, 341–348.
(24) Wang, Y.; Li, H. R.; Feng, Y.; Zhang, H. J.; Calzaferri, G.; Ren, T. Z. *Angew. Chem., Int. Ed.* **2010**, *49*, 1434–1438.
(25) Gago, S.; Fernandes, J. A.; Rainho, J. P.; Ferreira, R. A. S.; Pillinger, M.; Valente, A. A.; Santos, T. M.; Carlos, L. D.; Ribeiro-Claro, P. J. A.; Gonçalves, I. S. *Chem. Mater.* **2005**, *17*, 5077–5084.
(26) Li, Y.; Yan, B.; Yang, H. *J. Phys. Chem. C* **2008**, *112*, 3959–3968.
(27) Guo, X. M.; Guo, H. D.; Fu, L. S.; Deng, R. P.; Chen, W.; Feng, J.; Dang, S.; Zhang, H. J. *J. Phys. Chem. C* **2009**, *113*, 2603–2610.
(28) Minoofar, P. N.; Dunn, B. S.; Zink, J. I. *J. Am. Chem. Soc.* **2005**, *127*, 2656–2665.
(29) Zhao, D.; Seo, S. J.; Bae, B. S. *Adv. Mater.* **2007**, *19*, 3473–3479.
(30) Guo, X. M.; Wang, X. M.; Zhang, H. J.; Fu, L. S.; Guo, H. D.; Yu, J. B.; Carlos, L. D.; Yang, K. Y. *Microporous Mesoporous Mater.* **2008**, *116*, 28–35.
(31) Nobre, S. S.; Brites, C. D. S.; Ferreira, R. A. S.; de Zea Bermudez, V.; Carcel, C.; Moreau, J. J. E.; Rocha, J.; Wong Chi Man, M.; Carlos, L. D. *J. Mater. Chem.* **2008**, *18*, 4172–4182.
(32) Nunes, S. C.; Planelles-Aragó, J.; Ferreira, R. A. S.; Carlos, L. D.; de Zea Bermudez, V. *Eur. J. Inor. Chem.* **2010**, in press, DOI: 10.1002/ejic.201000166.
(33) Lin, A.; Meyers, M. A. *Mater. Sci. Eng., A* **2005**, *390*, 27–41.

form fibers that ultimately self-assemble at the micrometer scale. Bundle to bow-tie shapes are produced with increasing Eu^{3+} amount. The voids between the fibers act as percolation channels for the release of ethanol. This work represents a unique opportunity to address the effect of the morphology on the photoluminescence features of hybrids as we have been able to synthesize, from the same precursor, two systems (**Eu@L12**[31] and **Eu@A12**) with approximately the same Eu^{3+} concentration (1%) but displaying completely different morphologies.

Experimental Section

Synthesis of the Hybrid Materials. A mixture of water (155.0×10^{-3} mL, 8.6 mmol), NH_4F (Fluka, 0.50 mg, 1.4×10^{-2} mmol) and europium chloride hexahydrate, $EuCl_3 \cdot 6H_2O$ (Aldrich, 0.38 g, 1.1 mmol or 0.75 g, 2.0 mmol for **Eu@A12−1** and **Eu@A12−2** respectively) was added to a solution of **P12** (1.00 g, 1.4 mmol) in ethanol (EtOH, 5.0 mL, 86.0 mmol). The molar ratio of the reactants was the following: **P12**/EtOH/H_2O/NH_4F/$EuCl_3 \cdot 6H_2O$ = 1/60/6/0.01/y (y = 0.73 for **Eu@A12−1** and 1.42 for **Eu@A12−2**). The initially clear solution was stirred for 30 min and was left standing for 3 days. Gelation occurred within 24 h. The gel was successively washed with water, EtOH, acetone and was freeze-dried overnight. White powders were obtained in all cases.

The elemental analysis for the Eu^{3+}-containing hybrids revealed amounts of 0.74 and 1.31% of Eu^{3+} and 11.2 and 11.1% of Si for **Eu@A12−1** and **Eu@A12−2**, respectively. The Eu/chain ratio was 1/41 and 1/24 for **Eu@A12−1** and **Eu@A12−2** respectively.

Characterization. *X-ray Diffraction* (*XRD*). The XRD patterns were recorded using a Philips X'Pert MPD powder X-ray diffractometer. The samples were exposed to the Cu Kα radiation (1.54 Å) in a 2θ range between 1 and 60° with a step of 0.05 and time acquisition of 40 s per step.

Scanning Electronic Microscopy (*SEM*). The SEM images were obtained with a JEOL 6300F microscope and a Hitachi S-4500 apparatus after platinum metallization. X-ray microanalysis was performed to study the distribution of chemical composition (elemental maps) using a Bruker AXS Quantax 400 energy dispersive X-ray spectrometry system connected to a Hitachi SU-70 FEG-SEM apparatus. The samples for the analytical studies were coated with carbon.

Atomic Force Microscopy (*AFM*). The AFM measurements were performed using a Veeco "Multimode" AFM with Nanoscope IIIA controller. The topography images were recorded in the tapping modes on scan areas of 2×2 to 6×6 mm^2. The imaging conditions (set point, gains, driving frequency, and driving amplitude) were routinely set using standard procedures for tapping modes. The scan velocity was always kept at 0.5 Hz (12 mm·s^{-1}).

Elemental Analysis. The Eu and Si content were obtained by inductively coupled plasma optical emission spectroscopy (ICP-OES) analysis on a Jobin Yvon Activa-M instrument with a glass concentric nebulizer. For the Eu analysis the samples were digested under microwaves with 6 mL of hydrochloric acid (HCl), 2 mL of nitric acid (HNO_3), and 1 mL of hydrofluoric acid (HF) at 150 °C and dried. The F^- ion was removed by two successive additions of 5 mL of HCl after evaporation. The solution was recovered in 10 mL of HNO_3 20% and diluted. For the Si analysis the samples were digested under microwaves with 6 mL of HCl, 2 mL of HNO_3, and 1 mL of HF and diluted. The method is accurate within 10%.

Fourier Transform Infrared (*FT-IR*). The FT-IR spectra were acquired using a Mattson Mod 7000 spectrometer. The spectra were collected in the 4000−400 cm^{-1} range by averaging 64 scans at a resolution of 4 cm^{-1}. The solid samples (~2 mg) were finely ground and mixed with ~175 mg of dried KBr (Merck, spectroscopic grade) and pressed into pellets. Prior to recording the spectra the pellets were stored under vacuum for about 24 h at approximately 60 °C to reduce the levels of adsorbed water.

^{29}Si and ^{13}C Magic-Angle Spinning (*MAS*) *Nuclear Magnetic Resonance* (*NMR*). ^{13}C and ^{29}Si solid-state NMR spectra were obtained from Bruker FT-AM 200 or FT-AM 400 spectrometers by using cross-polarization (CP) and magic-angle spinning techniques (MAS). Tetramethylsilane (TMS) was used as reference for the chemical shifts.

Photoluminescence. Emission and excitation spectra were recorded at room temperature with a modular double grating excitation spectrofluorimeter (fitted with a 1200 grooves.mm^{-1} grating blazed at 330 nm) with a TRIAX 320 emission monochromator (fitted with a 1200 grooves.mm^{-1} grating blazed at 500 nm), FluoroLog-3, 2-TRIAX Horiba Scientific, coupled to a R928 Hamamatsu photomultiplier, using the front face acquisition mode. The excitation source was a 450W Xe arc lamp. The emission spectra were corrected for detection and optical spectral response of the spectrofluorimeter, and the excitation spectra were corrected for the spectral distribution of the lamp intensity using a photodiode reference detector. Time-resolved measurements were carried out with the setup described for the luminescence spectra using a pulsed Xe−Hg lamp (6 μs pulse at half width and 20−30 μs tail).

Absolute Emission Quantum Yields. The quantum yields were measured at room temperature using a quantum yield measurement system C9920−02 from Hamamatsu with a 150 W xenon lamp coupled to a monochromator for wavelength discrimination, an integrating sphere as sample chamber, and a multi channel analyzer for signal detection. Three measurements were made for each sample so that the average value is reported. The method is accurate within 10%.

Results and Discussion

Structural Description. The SEM images of the **A12**, **Eu@A12−1**, and **Eu@A12−2** hybrids are depicted in Figure 1. The SEM images of **A12** reveal irregular spherical shape morphology (3.0 to 10.0 μm in diameter) with a rough surface composed of plates (Figure 1a). We note that this morphology differs from that previously reported[20] because of the lack of thermal treatments in the current study. In the case of the Eu^{3+}-containing hybrids bundles of twisted fibers (3.0−4.0 μm long and 0.5−1.0 μm width) are observed for **Eu@A12−1** (Figure 1b). In the case of **Eu@A12−2** (Figure 1c), these bundles grow thicker (1.0−3.0 μm width) with increasing amount of Eu^{3+}, although their length remains unaffected. The resulting bow-tie structure exhibits at the tips a hollow substructure composed of channels with a diameter of ~0.1 μm (Figure 1c). These observations demonstrate that the Eu^{3+} content plays a key role in the structuring of the **A12** materials. It is

(34) Luz, G. M.; Mano, J. F. *Phil. Trans. R. Soc. A* **2009**, *367*, 1587–1605.

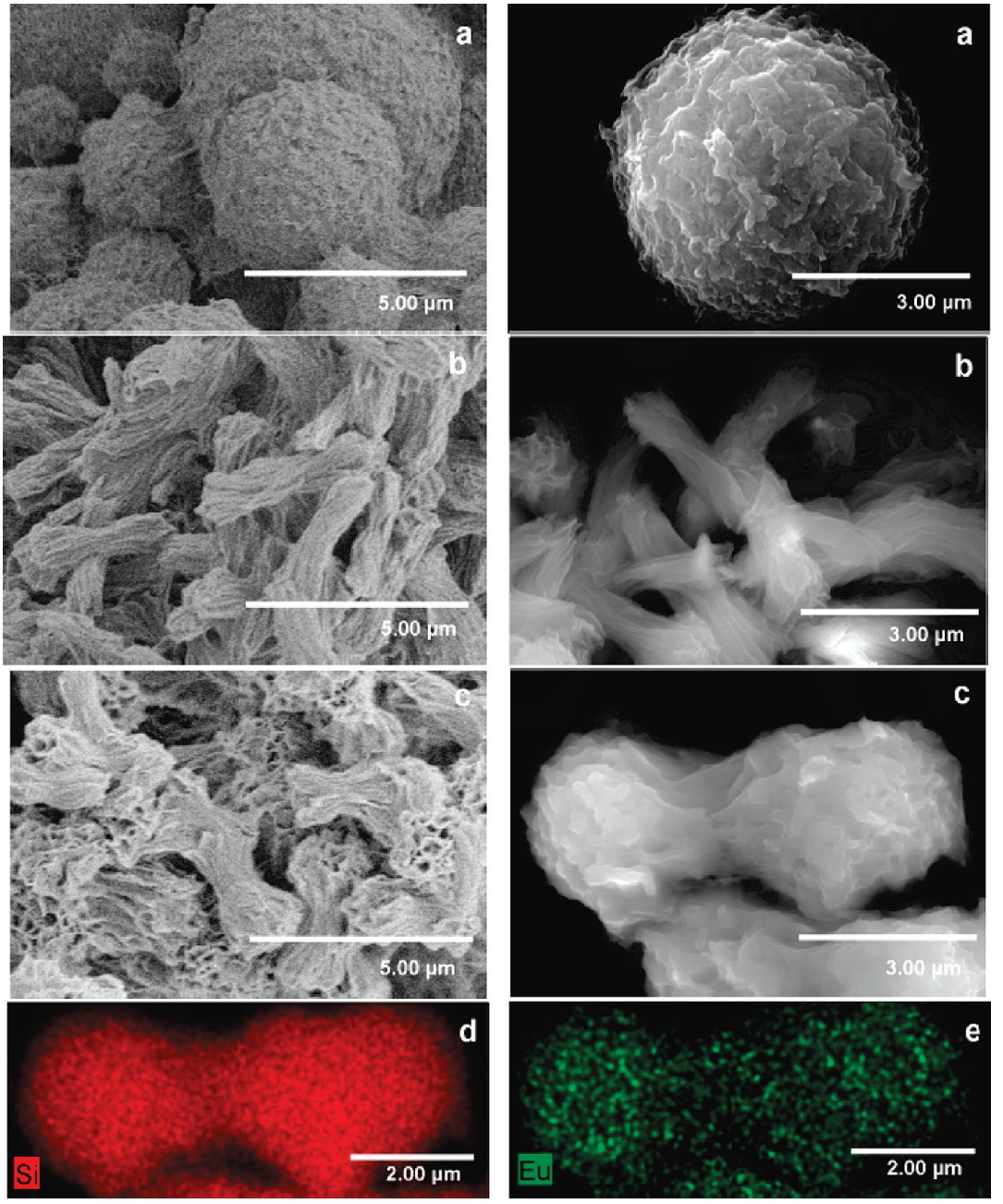

Figure 1. SEM images of (a) **A12**, (b) **Eu@A12−1**, and (c) **Eu@A12−2** hybrids and EDX of the **Eu@A12−2** hybrid for (d) Si and (e) Eu.

noteworthy that Eu and Si atoms are homogeneously distributed at the surface of these bow-tie microobjects in regions with an average size of ~200 nm, as evidenced by the X-ray mapping of the relative Si and Eu contents performed on **Eu@A12−2** (Figures 1d and 1e).

A more detailed view of the surface of the hybrids was obtained using AFM (Figure 2). Figure 2a shows that the surface of **A12** consists of long and irregular plates aligned along a single axis. In the AFM image of **Eu@A12−1** (Figure 2b), which reveals two microfibers separated by a grain boundary, the presence of regular thin flakes (166 ± 30 nm ×353 ± 90 nm) that tend to pile up and align along the microfibers' axis, in a brick-to-brick like arrangement, are clearly evident. Such organization is less obvious, however, on the surface of the bow-tie shape of **Eu@A12−2** (Figure 2c), with slightly bigger flakes (195 ± 15 nm ×410 ± 25 nm).

The solid state ^{29}Si CP-MAS NMR spectra (Figure S1 of Supporting Information) of the three hybrids exhibit resonances centered at −47.9, −57.1, and −67.0 ppm, ascribed to $R'Si(OSi)_1(OH)_2$ (T_1), $R'Si(OSi)_2(OH)$ (T_2), and $R'Si(OSi)_3$ (T_3) silicon environments, respectively. The absence of signals attributable to *Q*-type Si atoms demonstrates the total preservation of the Si−C covalent bonds. The condensation degree ($c = 1/3(\%T_1 + 2\%T_2 + 3\%T_3)$) determined for **A12** (91%) indicates that the material is almost fully condensed. For **Eu@A12−1** and **Eu@A12−2** the *c* value decreases to 65 and 63%, respectively, an indication that the dominating silicon sites are T_2, as already observed for other organic−inorganic hybrids synthesized in the presence of Eu^{3+}.[35]

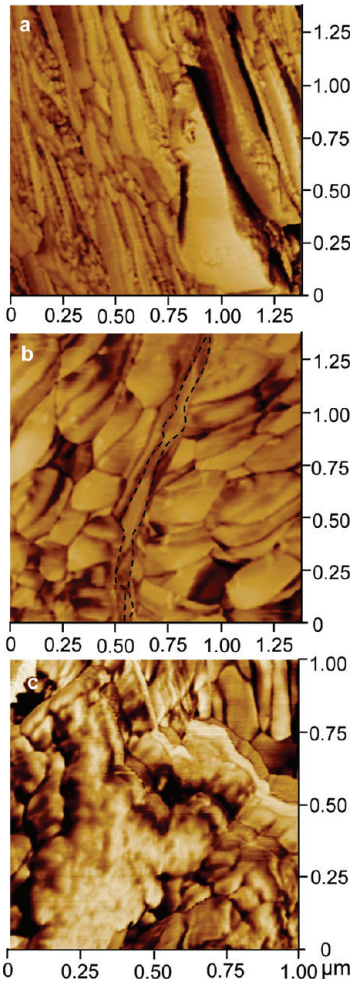

Figure 2. AFM image of (a) **A12**, (b) **Eu@A12−1**, and (c) **Eu@A12−2** hybrids. The dashed line indicates the grain boundaries between two microfibers.

The signals at 10.0−12.0 ppm found in the ^{13}C CP-MAS NMR spectra (Figure S2 of Supporting Information), ascribed to CH_2−Si carbons, represent an additional proof of the conservation of the covalent bonding established between the organic fragment and the siloxane network. The characteristic resonance of the urea groups at 159.9 ppm confirms the presence of the cross-links in the final materials. The propyl and alkyl chains also remain unaffected in the final materials, as demonstrated by the presence of the carbon resonances at 41.9−43.0 ppm (CH_2−N) and 30.3−31.5 ppm (alkyl chain). As previously reported,[36] the 30.0−35.0 ppm region reflects the distribution of the conformations of the methylene groups, the densely packed *all-trans* chains producing a peak centered at 34.0 ppm, whereas the amorphous regions characterized by *gauche* conformations yield a more shielded peak (~30.0 ppm). In contrast with the methylene groups of **A12**, which resonate mostly at 30.0 ppm, with practically no contribution at 34.0 ppm, those of **Eu@A12−1** and **Eu@A12−2** appear at 31.3 and

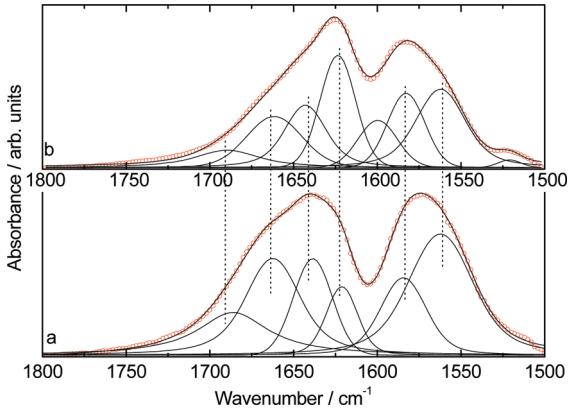

Figure 3. FT-IR spectra in the "amide I" and "amide II" regions of (a) **A12** and (b) **Eu@A12−1** hybrids.

33.9 ppm, respectively, evidencing the coexistence of highly packed and ordered *all-trans* chains with disordered *gauche* conformers. The narrowing of the urea signal at 159.9 ppm is another evidence of the ordering of the structure of the Eu^{3+}-doped hybrids. The full-width-at-half-maximum (fwhm) of this resonance decreases from 3.2 ppm in **A12** to 2.4 ppm in **Eu@A12−2**, indicating a smaller dispersion of environments around the non-coordinated urea groups.

Further information about the urea groups environments can be obtained through the analysis of the "amide I" (1800−1600 cm^{-1}) and "amide II" (1600−1500 cm^{-1}) bands of the FT-IR spectra.[37,38] The results of the curve-fitting performed in both regions of **A12** and **Eu@A12−1** are represented in Figure 3 (the spectrum of **Eu@A12−2**, not shown, is very similar to that of **Eu@A12−1**). The "amide I" band (mainly associated with C=O stretching vibrations[39]) of **A12** was decomposed into four components situated at approximately 1686, 1662, 1638, and 1622 cm^{-1} (Figure 3). These components are assigned to the absorption of C=O groups involved in ordered hydrogen-bonded urea−urea associations of increasing strength. The component associated with the absorption of "free" urea groups (i.e., urea groups in which the N−H or C=O groups are free from any hydrogen bonding interactions), expected at 1751 cm^{-1}, is absent in the "amide I" region of **A12** and **Eu@A12−1**, indicating that, independently of Eu^{3+} addition, all the urea groups of the **A12** framework are deeply involved in the formation of the hydrogen-bonded array. When the synthesis is performed with Eu^{3+} ions, a new component centered at 1600 cm^{-1} arises. This event is ascribable to the vibration of C=O groups strongly coordinated to Eu^{3+} ions, a proof of the effective interaction between the hybrid host and the lanthanide metal centers.

The XRD pattern of **A12** is dominated by a peak at 2.97 nm^{-1} and a hump centered at 14.70 nm^{-1} (Figure 4). When the sol−gel synthesis is performed in the presence

(35) Fu, L. S.; Ferreira, R. A. S.; Silva, N. J. O.; Fernandes, J. A.; Ribeiro-Claro, P.; Goncalves, I. S.; de Zea Bermudez, V.; Carlos, L. D. *J. Mater. Chem.* **2005**, *15*, 3117–3125.
(36) Clauss, J.; Schmidtrohr, K.; Adam, A.; Boeffel, C.; Spiess, H. W. *Macromolecules* **1992**, *25*, 5208–5214.
(37) de Zea Bermudez, V.; Carlos, L. D.; Alcácer, L. *Chem. Mater.* **1999**, *11*, 569–580.
(38) Nunes, S. C.; de Zea Bermudez, V.; Ostrovskii, D.; Carlos, L. D. *J. Mol. Sctruct.* **2004**, *702*, 39–48.
(39) Skrovanek, D. J.; Howe, S. E.; Painter, P. C.; Coleman, M. M. *Macromolecules* **1985**, *18*, 1676–1683.

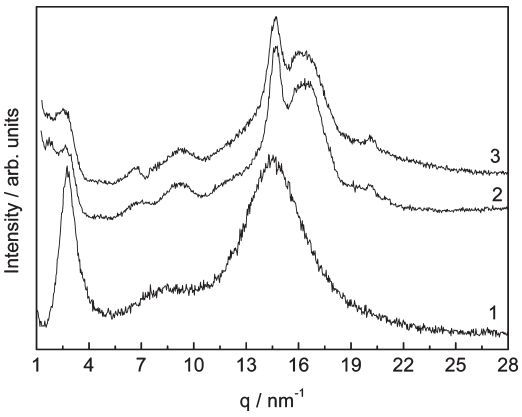

Figure 4. XRD patterns of the (1) **A12**, (2) **Eu@A12−1**, and (3) **Eu@A12−2** hybrids.

of $EuCl_3 \cdot 6H_2O$, the peak at lower q values, corresponding to the separation between siliceous domains which is governed by the alkyl chains length,[12,20,23] shifts to 2.65 nm^{-1} and 2.51 nm^{-1} for **Eu@A12−1** and **Eu@A12−2**, respectively, indicating an increase of the mean chain length. The calculated characteristic interlamellar spacing d ($d = 2\pi/q$) values of 2.25 ± 0.01 nm (**A12**), 2.37 ± 0.01 nm (**Eu@A12−1**), and 2.50 ± 0.01 nm (**Eu@A12−2**) are in good agreement with the increase in the proportion of *all-trans* conformations observed in NMR data. Unfortunately these peaks are located in the beam-stop and appear as shoulders of the latter and hence do not allow the calculation of coherence lengths and the subsequent comparison with that of the **A12** hybrid. The broad peak of **A12** at 14.53 nm^{-1} results from the overlap of (i) the separation between two neighboring urea groups in the self-associated urea−urea hydrogen-bonded array,[12,20,23,31] (ii) ordering within the siloxane domains[23,31] and (iii) chain−chain spacing.[20,23,31] Upon Eu^{3+} incorporation this broad band is split into two peaks, a finding that suggests a higher degree of structuring in the doped hybrids. Deconvolution procedures using Gaussian functions allowed us to identify in the XRD patterns of **Eu@A12−1** and **Eu@A12−2** three components at 13.08 nm^{-1} (separation between two neighboring urea groups, d_1 = 0.480 nm), 14.64 nm^{-1} (ordering within the siloxane domains, d_2 = 0.426 nm) and 16.41 nm^{-1} (chain−chain spacing d_3 = 0.383 nm). Taking in account the experimental error (0.01 nm), these distances are quite similar to those estimated for the lamellar **Eu@L12−1** hybrid.[31] In addition, the **Eu@A12** hybrids also produce three diffraction peaks at 6.77, 9.29, and 20.41 nm^{-1}, which have not been assigned yet (Figure 4).

Mechanistic Interpretation of the Formation of the Eu^{3+}-Based Hybrids. In our previous study,[31] highly ordered lamellar **L12** and **Eu@L12** hybrids were obtained from the **P12** precursor using HCl as catalyst and a large excess of water (R = 300) in the absence or presence of Eu^{3+} ions. In the present work a marked ordering of the hybrid structure is observed when the NH_4F-catalyzed synthesis is carried out in the presence of $EuCl_3 \cdot 6H_2O$ and R = 6. However, in contrast with the related lamellar **Eu@L12** hybrids, the **Eu@A12** hybrids do not exhibit any sharp XRD peak at low q values and consequently no lamellar features. A thorough comparison of the XRD, NMR, and FT-IR data of the **A12** and **L12** systems is available as Supporting Information (Figures S2−S4). The main consequence resulting from the presence of Eu^{3+} ions during the synthesis of the **A12** hybrids is the increase of the mean chain length which leads to a more regular stacking of the alkyl chains. This is evidenced in the XRD patterns of **Eu@A12** hybrids by the appearance of a well-defined peak at 16.41 nm^{-1} and in the corresponding ^{13}C NMR spectra by the enhancement of the signal at 34.0 ppm, attributable to an *all-trans* arrangement of the alkyl chains, as discussed above.

The higher degree of organization of the chains in **Eu@A12−1** and **Eu@A12−2** with respect to **A12** is mainly explained by a reinforcement of the hydrogen bonds between the urea groups. In parallel to the smaller dispersion of the urea groups' environment, evidenced by the sharp peak at 159.9 ppm in the ^{13}C NMR spectrum of **Eu@A12−1** (Figure S2 of Supporting Information), the results of the deconvolution of the "amide I" region of the FT-IR spectra of **A12** and **Eu@A12−1** show that the incorporation of Eu^{3+} ions during the synthesis results in a higher contribution of the strongest hydrogen-bonded associations at the expense of the destruction of the weaker ones, as already observed in the Eu^{3+}-doped diureasils.[40] Hence it is clear that the Eu^{3+} ions play a dual role in the **Eu@A12** materials acting not only as active emitting species but also as templates, being responsible for the short-range structuring of these materials. Similar metal-hybrid interactions have already been observed with palladium salts which have been reported to assist the fast formation of sol−gel hybrids through a palladium-complexed alkene system.[41]

We believe that the structure directing effect of the Eu^{3+} ions is intimately associated with the presence of the two available types of coordinating sites provided by the reacting **P12** precursor itself: the oxygen atoms of the Si−OH groups naturally formed during the hydrolysis and the C=O oxygen atoms of the urea groups inherent to the starting **P12** molecule. Under neutral conditions the mechanism of the F^- ion catalysis in sol−gel processes of $Si(OR)_4$ compounds is known to occur via an S_N2 mechanism where anionic intermediates are formed before the condensation steps with the F^- ion acting as nucleophile.[42−44] Negatively charged penta- and hexavalent silicon intermediates are formed and a water molecule can induce a nucleophilic substitution of the OR group.[45] For the **Eu@A12** hybrids we propose that the

(40) de Zea Bermudez, V.; Ostrovskii, D.; Gonçalves, A. C.; Lavoryk, S.; Carlos, L. D.; Ferreira, R. A. S. *J. Phys. Chem. B* **2005**, *109*, 7110–7119.
(41) Corriu, R. J. P.; Moreau, J. J. E.; Thépot, P.; Wong Chi Man, M. *J. Mater. Chem.* **1994**, *4*, 987–989.
(42) Tilgner, I. C.; Fischer, P.; Bohnen, F. M.; Rehage, H.; Maier, W. F. *Microporous Mater.* **1995**, *5*, 77–90.
(43) MrowiecBialon, J.; Pajak, L.; Jarzebski, A. B.; Lachowski, A. I.; Malinowski, J. J. *Langmuir* **1997**, *13*, 6310–6314.
(44) Corriu, R. J. P.; Guerin, C.; Moreau, J. J. E. *Top. Stereochem.* **1984**, *15*, 43–198.
(45) Brefort, J. L.; Corriu, R. J. P.; Guerin, C.; Henner, B. J. L.; Wongchiman, W. W. C. *Organometallics* **1990**, *9*, 2080–2085.

Scheme 2. Tentative Representation of the Mechanism of Formation of Eu@A12 in the (a) Early and (b) Late Stages[a]

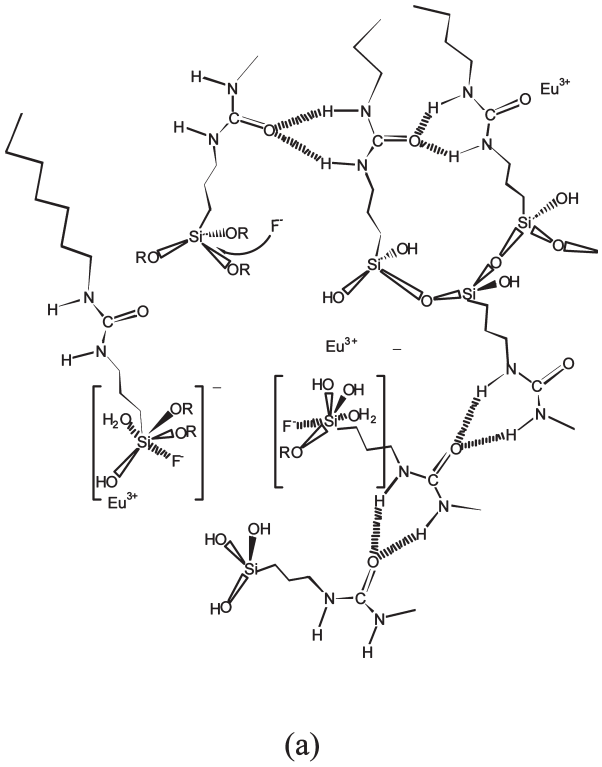

(a)

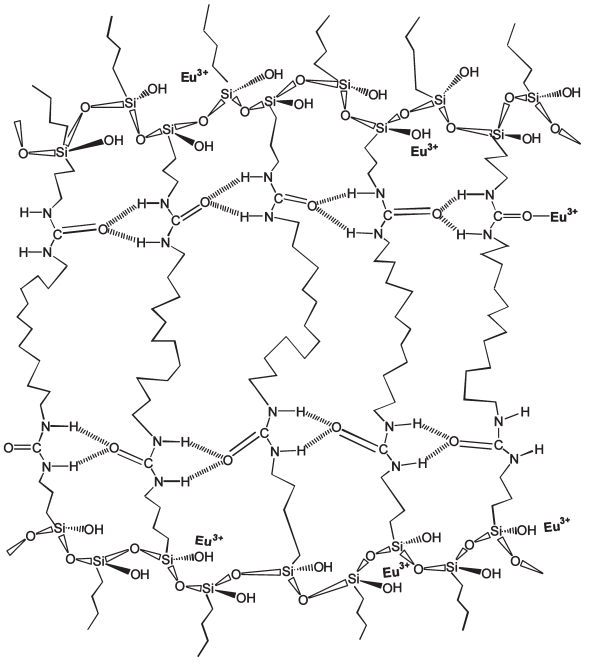

(b)

[a] In these schemes the other ligands of the Eu^{3+} ion coordination sphere (e.g., chloride ions, water molecules, and other carbonyl groups) have been omitted for the sake of clarity.

negative charge of the Si intermediate species will attract the Eu^{3+} ions because of electrostatic interactions (Scheme 2a). These cations will remain bonded to the oxygen atoms of the Si−OH groups even after elimination of EtOH and F^- ion in the last step of the mechanism.

In parallel to this anchoring process undergone by a fraction of the incorporated emitting species, some of the remaining Eu^{3+} ions will bind to the carbonyl oxygen atoms of the urea groups. This interaction will induce a more positive charge over the urea NH proton, thus promoting the formation of additional hydrogen-bonds with neighboring urea groups over the whole reaction medium. A strong and ordered hydrogen-bonded array will eventually build up. The direct consequence of the formation of these bifurcated hydrogen-bonded aggregates will be the stacking of the hydrophobic alkyl chains into flakes (Scheme 2b). Neighboring flakes will then spontaneously self-assemble. At this point of supramolecular self-assembly, thin and regular nanometer-size flakes (150−400 nm long) will be produced. As shown in Figure 1e, the Eu^{3+} ions are homogeneously distributed in regions with size dimensions (> 200 nm) compatible with the length range of these flakes, supporting therefore the reduction of the growth (condensation) rate of the siloxane network because of the suppressing role of the Eu^{3+} ions. Owing to their regular size, these anisotropic flakes will easily pile up along one dimension to form micrometric assemblies along a brick-to-brick like arrangement (Figure 5) similarly to nature-existing aragonite in a much higher dimension (10.0−20.0 μm wide and 0.5 μm thick),[33,46] thus explaining the axial symmetry of the resulting uniform microsize (up to 4 μm) fibers. Finally, the fibers stack together into bundles as a result of microscopic self-assembly (Figure 1b and 1c).

Hence, the inhibitor effect of the Eu^{3+} ions bonded to Si−OH groups aided by Eu^{3+}−mediated hydrogen bonding formation combined, in turn, with supramolecular and micrometer self-assembly processes account for the different morphologies observed: spheres in the case of **A12**, bundles and bow-tie shapes composed of twisted fibers in the case of **Eu@A12−1** and **Eu@A12−2**, respectively.

In **A12** random stacking of the non-uniform 0.3−1.0 μm size plates and isotropic growth account for the spherical shape (Figure 1a).[47,48] The bow-tie shape of the **Eu@A12−2** probably results from a concerted template effect governed both by the EtOH release during the hydrolysis−condensation reactions and the Eu^{3+}-bridged interfiber cross-links. Indeed the flow of EtOH is likely to increase from the core to the tips of the bow-tie objects as the liquid travels through the fibers (Figure 5). This sort of expansion effect is typically associated with the release of the internal stresses (shearing) a solvent is subject to when it is forced to go through a confined space. At high salt concentration, the Eu^{3+} ions have a third key role serving as cross-linkers of adjacent fibers (as discussed below), thus constraining the EtOH flow pathways and inducing the formation of the bow-tie.

(46) Bruet, B. J. F.; Qi, H. J.; Boyce, M. C.; Panas, R.; Tai, K.; Frick, L.; Ortiz, C. *J. Mater. Res.* **2005**, *20*, 2400–2419.
(47) Moreau, J. J. E.; Vellutini, L.; Wong Chi Man, M.; Bied, C. *Chem. Eur. J.* **2003**, *9*, 1594–1599.
(48) Pichon, B. P.; Wong Chi Man, M.; Dieudonné, P.; Bantignies, J. L.; Bied, C.; Sauvajol, J. L.; Moreau, J. J. E. *Adv. Funct. Mater.* **2007**, *17*, 2349–2355.

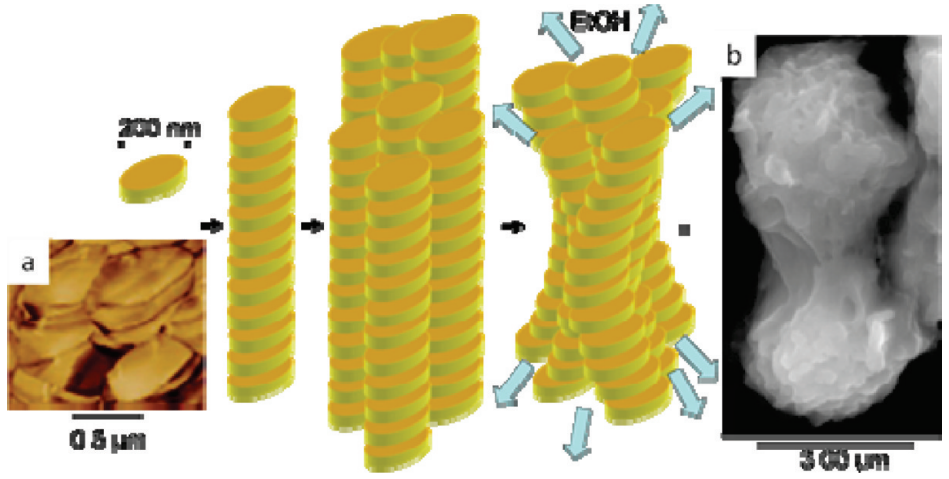

Figure 5. Schematic representation of the proposed mechanism for the formation of the bow-tie shaped **Eu@A12−2**. (a) AFM and (b) SEM images of the **Eu@A12−2** hybrid.

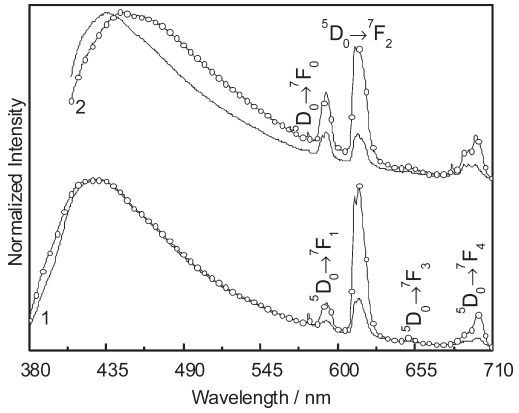

Figure 6. Emission spectra of the (line) **Eu@A12−1** and (circles) **Eu@A12−2** hybrids excited at (1) 360 nm and (2) 393 nm.

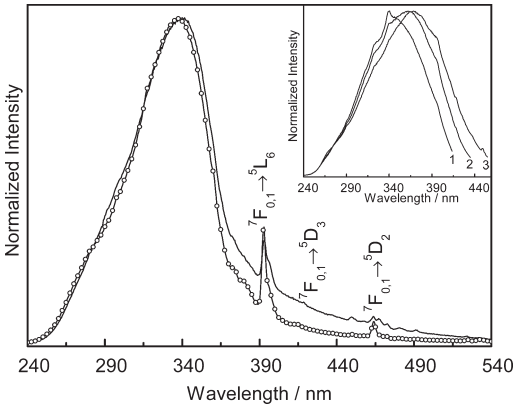

Figure 7. Excitation spectra of the (line) **Eu@A12−1** and (circles) **Eu@A12−2** hybrids monitored at 614 nm. The inset shows the excitation spectra of the **Eu@A12−1** hybrid monitored at (1) 430 nm, (2) 450 nm, and (3) 470 nm.

In the SEM pictures of Figure 1c the hollow channels (up to 0.5 μm diameter) sculpted by solvent release are perfectly visible at the far end of the fiber-made bow-tie structures.

Photoluminescence. Figure 6 displays the emission spectra of **Eu@A12−1** and **Eu@A12−2** excited at 360 and 393 nm. Both spectra consist of a series of straight lines ascribed to the intra-4f^6 $^5D_0 \rightarrow {}^7F_{0-4}$ transitions superimposed on a large broad band, whose energy deviates toward the red as the excitation wavelength increases (280−393 nm). A similar broad emission was also detected for the non doped **A12** host (Figure S5 of Supporting Information), the **L12** lamellar hybrid,[31] and similar amorphous hybrids.[23,49−54] This emission has been ascribed to the overlap of two distinct components mediated by donor−acceptor pair transitions that occur within the cross-linkages between the organic and the inorganic counterparts and within the siliceous skeleton, because of the presence of oxygen related defects, •O−O−Si≡(CO_2).[23,52,54] The relative intensity of the hybrids' emission band depends on the amount of Eu^{3+} incorporated (for higher Eu^{3+} concentrations a decrease in the intensity of the hybrids' host emission is observed) which suggests the presence of host-to-Eu^{3+} energy transfer, as previously observed in analogous amorphous hybrids.[50,55]

Figure 7 shows the excitation spectrum monitored within the $^5D_0 \rightarrow {}^7F_2$ transition (614 nm) for **Eu@A12−1**. The inset of this figure displays the excitation spectra monitored along the hybrid host emission (430−470 nm). These spectra resemble that of **A12** (inset in Figure S5 of Supporting Information) displaying a large broad band whose peak position depends on the monitoring wavelength. The excitation spectrum monitored within the Eu^{3+} lines reveals a large broad band peaking at 340 nm

(49) Carlos, L. D.; Messaddeq, Y.; Brito, H. F.; Ferreira, R. A. S.; de Zea Bermudez, V.; Ribeiro, S. J. L. *Adv. Mater.* **2000**, *12*, 594–598.
(50) Ferreira, R. A. S.; Carlos, L. D.; Gonçalves, R. R.; Ribeiro, S. J. L.; de Zea Bermudez, V. *Chem. Mater.* **2001**, *13*, 2991–2998.
(51) Molina, C.; Dahmouche, K.; Messaddeq, Y.; Ribeiro, S. J. L.; Silva, M. A. P.; de Zea Bermudez, V.; Carlos, L. D. *J. Lumin.* **2003**, *104*, 93–101.
(52) Carlos, L. D.; Ferreira, R. A. S.; de Zea Bermudez, V.; Ribeiro, S. J. L. *Adv. Funct. Mater.* **2001**, *11*, 111–115.
(53) Nunes, S. C.; de Zea Bermudez, V.; Cybinska, J.; Ferreira, R. A. S.; Legendziewicz, J.; Carlos, L. D.; Silva, M. M.; Smith, M. J.; Ostrovskii, D.; Rocha, J. *J. Mater. Chem.* **2005**, *15*, 3876–3886.
(54) Carlos, L. D.; Ferreira, R. A. S.; Pereira, R. N.; Assunção, M.; de Zea Bermudez, V. *J. Phys. Chem. B* **2004**, *108*, 14924–14932.
(55) Nobre, S. S.; Lima, P. P.; Mafra, L.; Ferreira, R. A. S.; Freire, R. O.; Fu, L. S.; Pischel, U.; de Zea Bermudez, V.; Malta, O. L.; Carlos, L. D. *J. Phys. Chem. C* **2007**, *111*, 3275–3284.

and a high-wavelength component between 360 and 540 nm superimposed on a series of Eu^{3+} transitions between the $^7F_{0,1}$ levels and the $^5L_6$ and $^5D_{3,2}$ excited states. The main component may be ascribed to the hybrid host excited states that transfer energy to the Eu^{3+} ions, as it overlaps the excitation spectra monitored within the hybrid host excited states (inset in Figure S5 of Supporting Information). The excitation spectrum of **Eu@A12−2** resembles that of **Eu@A12−1** (Figure 7).

The absolute emission quantum yields were measured for the non doped and Eu^{3+}-containing hybrids under distinct excitation wavelengths (280−393 nm). For the **A12** hybrid a maximum value of 0.24 ± 0.02 was reached under 290 nm excitation. This value is higher than that of the lamellar **L12** hybrid (0.14 ± 0.01),[31] pointing out that the distinct morphologies that result from different synthetic routes have an impact on the quantum yield value. In particular we note that a higher degree of organization induces a decrease in the emission quantum yield, as previously observed in amide-functionalized hybrids.[23,53] Moreover, the **A12** quantum yield value is higher than those reported for analogous amorphous diureasils (0.06−0.08 ± 0.01),[52,54] diurethanesils (0.19 ± 0.02),[52,54] and diamidosils (0.05 ± 0.01)[53] and for ordered monoamidosils (0.03 ± 0.01).[23]

The incorporation of Eu^{3+} into the **A12** hybrid induces a decrease in the absolute emission quantum yield values. In particular, a maximum value of 0.06 ± 0.01 was found for **Eu@A12−1** and **Eu@A12−2** under excitation via the hybrid host excited states (340−360 nm). This decrease in the quantum yield value is in good agreement with the existence of hybrid-to-Eu^{3+} energy transfer.[50,55]

Under direct intra-$4f^6$ excitation, the quantum yield values are lower than the detection limits of our equipment (< 0.01) reinforcing the active role of the hybrid host in Eu^{3+} sensitization. Comparing these values with those of analogous Ln^{3+}-containing organic−inorganic hybrids, the quantum yield values reported here, although smaller than that reported for Eu^{3+}-doped diureasils (0.13 ± 0.02),[50] are substantially higher than those observed for the **Eu@L12** lamellar hybrids (< 0.01).[31]

We stress that the photoluminescence measurements reported here were all carried out within 2 months after preparing fresh samples. When the samples are kept in ambient atmosphere the quantum yield values decrease (approximately 2.5 times in one year) and the relative intensity of the intra-$4f^6$ lines in **Eu@A12−1** and **Eu@A12−2** increases with aging time. However, both the overall broad emission of the hybrid host and the energy of the Eu^{3+} lines remain unaltered. The dependence of the quantum yield values and relative intra-$4f^6$ intensities on the aging time lies beyond the scope of the present work.

To get further insight into the Eu^{3+}-local coordination the intra-$4f^6$ emission lines were scanned with higher resolution. Figure 8a shows the $^5D_0 \rightarrow {}^7F_{0-4}$ transitions under excitation via the hybrid host' excited states (340 nm) and directly into the $^5L_6$ level (393 nm). Under 340 nm excitation the Eu^{3+} emission spectra display a

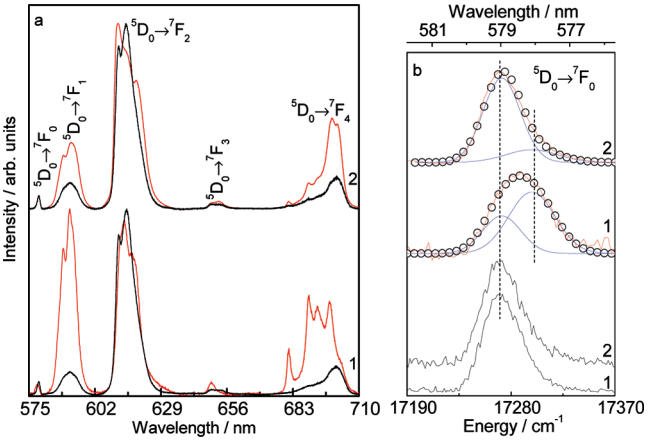

Figure 8. (a) High resolution emission spectra of the (1) **Eu@A12−1** and (2) **Eu@A12−2** hybrids excited at 340 nm (black line) and 393 nm (red line). (b) Magnification of the $^5D_0 \rightarrow {}^7F_0$ transition for the two hybrids. For 393 nm excitation the curve fit (represented by open circles) was performed using two Gaussian functions (solid blue lines).

single $^5D_0 \rightarrow {}^7F_0$ line and a *J*-degeneracy splitting of the $^7F_{1,2}$ levels into 3 and 4 Stark components, respectively. No changes in the energy and Stark splitting are observed upon varying the Eu^{3+} concentration (Figure 8), indicating that the Eu^{3+} ions occupy the same average local environment in **Eu@A12−1** and **Eu@A12−2** (labeled site A), involving Eu^{3+} coordination to the oxygen atoms of the C=O groups (as the above-mentioned structural results indicate), besides Cl^- ions and water molecules. Under 393 nm excitation the spectra drastically change (Figure 8) indicating the existence of a second Eu^{3+} local environment (labeled site B). Particularly a series of narrower Stark components becomes much more evident in the overall envelope of the $^5D_0 \rightarrow {}^7F_{1-4}$ transitions and the $^5D_0 \rightarrow {}^7F_2/{}^5D_0 \rightarrow {}^7F_1$ intensity ratio decreases significantly indicating the presence of a center of inversion. To further elucidate the origin of Eu^{3+} local site B, selectively excited under 393 nm, the energy and fwhm of the $^5D_0 \rightarrow {}^7F_0$ line was estimated both as function of the excitation wavelength (340 and 393 nm) and Eu^{3+} concentration. For an excitation of 340 nm, the $^5D_0 \rightarrow {}^7F_0$ line was fitted using a single Gaussian yielding the same energy and fwhm for **Eu@A12−1** and **Eu@A12−2**, 17272.4 ± 0.3 cm^{-1} and 34.0 ± 0.6 cm^{-1}, respectively (Figure 8b). However for an excitation of 393 nm, the $^5D_0 \rightarrow {}^7F_0$ transition is only well modeled by the sum of two Gaussian functions: one with the same energy and fwhm of that measured under 340 nm excitation and a high-energy component peaking at 17298.0 ± 2.5 cm^{-1} with a fwhm of 45.0 ± 5.5 cm^{-1}. The fact that the E_{00} value for site B is blue-shifted when compared with the energy of the $^5D_0 \rightarrow {}^7F_0$ transition assigned to Eu^{3+} ions in site A, points out a less covalent degree of the Eu−O bonds in Eu^{3+} site B.[56,57] As site B comprises the population of Eu^{3+} ions that are located at the surface of the siloxane network, the coordination sphere of these Eu^{3+}

(56) Malta, O. L.; Batista, H. J.; Carlos, L. D. *Chem. Phys.* **2002**, *282*, 21–30.
(57) Carlos, L. D.; Malta, O. L.; Albuquerque, R. Q. *Chem. Phys. Lett.* **2005**, *416*, 238–242.

ions may include several Si−OH groups. Consequently the number of OH groups in site B (originating from Si−OH groups and water molecules) will be considerably higher than that found in site A (originating from water molecules only). Comparing the relative intensity of the two $^5D_0 \rightarrow {}^7F_0$ transitions, we may unequivocally visualize a higher relative contribution of the Eu^{3+} ions located at site B for the less concentrated hybrid, **Eu@A12−1** (Figure 8B), in strong agreement with the mechanistic interpretation of the formation of the fiber-type structures described above. We may rationalize that the increase of Eu^{3+} content will increase the population of Eu^{3+} sites A. This effect will tend to approach the fibers leading to the formation of bundle- or ultimately bow-tie structures, as explained above. In this way, distinct fibers will be linked *via* bridging Eu^{3+} ions bonded to urea C=O groups belonging to distinct fibers.

Additional arguments supporting the assignment of the two distinct Eu^{3+}-local coordination groups, in particular the presence of Si−OH groups, may be retrieved from the analysis of the $^5D_0$ emission decay curves monitored under 340 and 393 nm excitation. Under 340 nm excitation all the curves are well described by a single exponential function, yielding lifetime values of 0.673 ± 0.017 ms and 0.536 ± 0.016 ms, for **Eu@A12−1** and **Eu@A12−2**, respectively. The smaller value found for the higher concentrated hybrid points out a higher non-radiative transition probability, as we will detail next. Under 393 nm, the emission decay curves are well modeled by a bi-exponential function. Considering that one of the lifetime values coincides with that determined under 340 nm excitation, the curve fitting yields a second value of 0.115 ± 0.011 and 0.060 ± 0.006 for **Eu@A12−1** and **Eu@A12−2**, respectively. The lower $^5D_0$ lifetime value obtained for the Eu^{3+} ions located in site B (when compared with that measured for site A excited at 340 nm) supports the above suggestion that this local environment involves metal coordination to a larger number of OH groups belonging to the Si−OH groups, leading to an increase in the non-radiative transition probability.

The estimation of the $^5D_0$ radiative (A_r) and non-radiative (A_{nr}) transition probabilities, and the $^5D_0$ quantum efficiency (η) [$\eta = A_r/(A_r + A_{nr}) = A_r/A_T$], of Eu^{3+} ions in site A were made based on the emission spectrum and $^5D_0$ lifetime.[9,31,49] We used the selective excitation of 340 nm, as the Eu^{3+} ions located in site B are only detected under intra-$4f^6$ excitation. The radiative contribution is calculated from the relative intensities of the $^5D_0 \rightarrow {}^7F_{0-4}$ transitions (the $^5D_0 \rightarrow {}^7F_{5,6}$ branching ratios are neglected because of their poor relative intensity with respect to that of the remaining $^5D_0 \rightarrow {}^7F_{0-4}$ lines). The $^5D_0 \rightarrow {}^7F_1$ transition does not depend on the local ligand field and thus may be used as a reference for the whole spectrum. An effective refractive index of 1.5 was used leading to $A_{01} \approx 50\ s^{-1}$, where A_{01} stands for the Einstein's coefficient of spontaneous emission between the $^5D_0$ and the $^7F_1$ Stark levels. The calculated values, gathered in Table 1, show a decrease in the η value from 0.37 to 0.26 as the concentration increases, a trend essentially related with an increase of the A_{nr} values.

Table 1. Experimental Lifetime (τ, ms), Radiative (A_r, ms^{-1}), Non-Radiative (A_{nr}, ms^{-1}) Transition Probabilities, $^5D_0$ Quantum Efficiency (η), Quantum Yield (Φ), $\Omega_{\lambda=2,4}$ Intensity Parameters ($\times 10^{-20}$ cm^2) and Number of Water Molecules Coordinated to the Eu^{3+} Ion (n_w) for Eu@A12-1, Eu@A12-2, and Eu@L12-1

hybrid	τ	A_r	A_{nr}	η	Φ	n_w	Ω_2	Ω_4
Eu@A12−1	0.673	0.549	0.937	0.37	0.06	0.7 ± 0.1	15.4	3.8
Eu@A12−2	0.536	0.482	1.384	0.26	0.06	1.2 ± 0.1	13.3	3.6
Eu@L12−1[31]	0.652	0.731	0.803	0.47	< 0.01	0.5 ± 0.1	20.1	5.1

The variations in η and A_{nr} values may be rationalized in terms of the number of water molecules coordinated to the Eu^{3+} ions ($n_w \pm 0.1$) based on the empirical formula reported by Supkowski and Horrocks.[58] The estimated values are 0.7 and 1.2 for the **Eu@A12−1** and **Eu@A12−2** hybrids, respectively. The small increase in the n_w value with the increase of the Eu^{3+} content is in good agreement with the arguments figured out previously concerning the minor variation of the Eu^{3+} first coordination shell in the **Eu@A12** hybrid. To further characterize the Eu^{3+}-local coordination the experimental values for the Ω_2, Ω_4 intensity parameters were determined (Table 1) following a methodology detailed elsewhere.[9] The relative high values of Ω_2, similar to those previously found in amorphous organic−inorganic hybrids, might be interpreted as a consequence of the hypersensitive behavior of the $^5D_0 \rightarrow {}^7F_2$ transition, suggesting that the dynamic coupling mechanism is quite operative and that the chemical environment is highly polarizable. In particular, a correlation has been noticed in the sense that compounds expected to have a higher degree of covalence tend to present higher values of Ω_2. As shown in Table 1, the Ω_2 values decrease slightly as the Eu^{3+} concentration increases, pointing out a small decrease in the average degree of covalency of the Eu−O bonds, in agreement with the conclusions mentioned before relatively to the minor variation of the Eu^{3+} first coordination shell in the two hybrids. These values are higher than those previously estimated for Eu^{3+}-doped diureasil[49] and **L12** hybrid hosts,[31] pointing out a higher degree of covalency for the Eu−O bonds in these hybrids.

The photoluminescence features of the **Eu@L12−1**[31] and **Eu@A12−1** hybrids synthesized from the same precursor with approximately the same Eu^{3+} concentration (1%), were compared to address the effect of the morphology in these features. The changes on the $^5D_0 \rightarrow {}^7F_0$ energy (site A, 17272.5 ± 0.2 cm^{-1} in **Eu@A12−1** and 17254.6 ± 0.3 cm^{-1} in **Eu@L12−1**[31]), $^5D_0$ lifetime, $^5D_0$ quantum efficiency, number of coordinated water molecules, Ω_2 values (Table 1) and $^5D_0 \rightarrow {}^7F_2/{}^5D_0 \rightarrow {}^7F_1$ intensity ratio (Figure S6 of Supporting Information), clearly indicate that the Eu^{3+} local neighborhood considerably depends on the overall morphology of the samples.

Conclusions

For the first time a short-range distance ordering yielding hierarchically structured bridged polysilsesquioxanes

(58) Supkowski, R. M.; Horrocks, W. D. *Inorg. Chim. Acta* **2002**, *340*, 44–48.

by means of an unprecedent Eu^{3+}-assisted process has been reported and characterized. The presence of the Ln^{3+} ions induces different morphologies (bundles and bow-tie shapes of twisted fibers built from flake-like BBs) that contrast with the spherical arrangement of small plates found in the **A12** pristine material. The fibers consist of nanometer-size flakes which pile up together along a brick-like tile-to-tile nacre-type arrangement. The latter stacking arrangement is only possible because of the regular size of the flakes. Their anisotropic shape is a direct consequence of the inhibitor effect played by some of the Eu^{3+} ions bonded to surface siloxane Si−OH groups (Eu^{3+} site B) thus suppressing the condensation of the inorganic network. Interestingly, the synthesis of the Eu^{3+}-doped hybrids involves the combination of classical F^--catalyzed sol−gel reactions with self-assembly processes that span several length scales. Supramolecular self-assembly, aided by strong urea−urea hydrogen-bonding interactions, will be active in the early steps of the formation of the hybrids. Microscale self-assembly alone or aided by bridging Eu^{3+} ions bonded to C═O groups located in different fibers (Eu^{3+} site A) that act as fiber cross-linkers, will be activated in the late steps of the synthesis giving rise to bundles at low Eu^{3+} concentration or bow-tie shapes at high Eu^{3+} concentration, respectively.

The **Eu@A12** hybrids are room temperature multiwavelength emitters because of the convolution of the hybrids' emitting centers and the intra-$4f^6$ transitions. The two distinct Eu^{3+} local sites (A and B) are clearly discerned in the emission spectra, being the Eu^{3+} first coordination shell in site A almost independent of the Eu^{3+} content—despite the minor variations found in the $^5D_0$ quantum efficiency (0.26−0.37), number of coordinated water molecules (0.7−1.2) and experimental intensity Ω_2 parameter ($15.4-13.3\times10^{-20}$ cm^2)—incorporating oxygen atoms of the carbonyl group, chloride atoms, and water molecules. Furthermore, the Eu^{3+} ions located in site B are characterized by (i) a series of narrower Stark components, (ii) a low $^5D_0\rightarrow{}^7F_2/{}^5D_0\rightarrow{}^7F_1$ intensity ratio (indicating the presence of a center of inversion), (iii) a blue-shifted E_{00} value (when compared with that associated with the Eu^{3+} ions in site A) that points out a less covalent degree of the Eu−O bonds, and (iv) a lower $^5D_0$ lifetime value. All this evidence supports the suggestion that the Eu^{3+} ions in site B are coordinated to Si−OH groups (with therefore a higher number of OH oscillators, relatively to the typical number in site A). The relative contribution of the Eu^{3+} ions located in site B decreases as Eu^{3+} concentration increases reflecting the establishment of Eu^{3+}-mediated interfiber cross-links leading to the formation of bow-tie structures.

Furthermore, as hybrids with approximately the same Eu^{3+} concentration (∼1%) but with completely different morphologies (**Eu@L12−1** and **Eu@A12−1**) were synthesized from the same precursor, this family of hierarchically structured bridged silsesquioxanes represents a unique example in which the effect of the morphology on the photoluminescence features could be addressed in great detail. The results point out that the Eu^{3+} local neighborhood considerably depends on the overall morphology of the samples, sensing therefore the structural changes induced by the acid- or F^--based catalyst and R ratio used. A comprehensive understanding of how the unprecedent role of Eu^{3+} in the modulation of the morphology of organic−inorganic hybrids at different length scales can be generalized to other functional active centers will surely contribute to optimize the rational shaping and therefore the functionality of those materials opening up exciting new directions in materials science nanoengineering.

Acknowledgment. The support of NoE FAME, Fundação para a Ciência e Tecnologia (FCT), FEDER, LUSO and PHC-PESSOA (Ministère des Affaires Étrangères et Européennes) is gratefully acknowledged. The authors would like to thank the collaboration of A. G. Macedo and M. C. Ferro, Aveiro University, for the AFM and SEM measurements, respectively. S.S.N. thanks FCT grant (SFRH/BD/28739/06).

Supporting Information Available: Figures S1−S6. This material is available free of charge via the Internet at http://pubs.acs.org.